Estimation of the aerodynamic roughness length in arid and semi-arid regions over the globe with the ERS scatterometer

Catherine Prigent,[1] Ina Tegen,[2] Filipe Aires,[3] Béatrice Marticorena,[4] and Merhez Zribi[5]

Received 20 August 2004; revised 15 November 2004; accepted 7 February 2005; published 11 May 2005.

[1] Estimates of the aerodynamic roughness lengths z_0 in arid and semi-arid regions are for the first time provided for the whole globe, using satellite ERS scatterometer observations. A statistical relationship is derived between the ERS scatterometer backscattering coefficients and quality in situ and geomorphological z_0 estimates. It is a practical solution to provide realistic roughness maps with large-scale spatial patterns that are consistent with independent surface characterization. In addition, it makes it possible to analyze the seasonal and interannual variations of this parameter on a global basis. The satellite-derived surface roughness parameters have been implemented into the dust emission scheme of a global dust cycle model. Dust emission computations are improved when using the ERS derived z_0 as input parameter. The spatial correlation between the TOMS observation frequency and the model dust events increases from 0.34 when using fixed z_0 to 0.52 when using the satellite-derived estimates.

Citation: Prigent, C., I. Tegen, F. Aires, B. Marticorena, and M. Zribi (2005), Estimation of the aerodynamic roughness length in arid and semi-arid regions over the globe with the ERS scatterometer, *J. Geophys. Res.*, *110*, D09205, doi:10.1029/2004JD005370.

1. Introduction

[2] Land surface roughness can be characterized by the aerodynamic roughness length z_0 which is defined as the height above a surface at which the wind profile is assumed to be zero. Land surface roughness is a key factor in mineral dust emission process. It affects both the quantity of potentially eroded material and the minimum wind speed required to raise the dust particles [*Gillette and Passi*, 1988]. While the threshold velocity required to initiate dust emission is increased in areas with higher surface roughness compared to smooth surfaces, the drag coefficient is also increased, leading to higher wind friction and thus possibly to higher dust emissions. Among the various atmospheric aerosols, mineral dusts in arid and semi-arid regions are the most abundant (~40% [*Intergovernmental Panel on Climate Change* (*IPCC*), 1995]), playing an important but complex role in the atmospheric radiation budget with a net global impact (cooling or warming) still debated [*IPCC*, 2001]. In order to evaluate their impact, efforts are conducted to model the dust cycles [e.g., *Joussaume*, 1990; *Tegen and Fung*, 1994; *Tegen et al.*, 2000], requiring a description of the aeolian process. Physical models of mineral dust emissions have thus been recently developed based on an explicit description of the main physical processes involved during dust production [*Marticorena and Bergametti*, 1995; *Shao et al.*, 1996; *Alfaro and Gomes*, 2001; *Shao*, 2001]. They include parameterizations of the erosion threshold as a function of the surface roughness parameters. For example, *Marticorena and Bergametti* [1995] have developed a dust emission model including a parameterization of the threshold wind friction velocity U^*_t as a function of the aerodynamic roughness length z_0. This parameterization was found to reproduce satisfactorily the thresholds of erosion measured on a variety of natural surfaces [*Marticorena et al.*, 1997]. However, the use of such physical models are up to now limited by the availability of data sets characterizing the surface features of the arid and semi-arid areas, especially their aerodynamic roughness length. Global models of the dust cycle usually use either a globally constant surface roughness to compute dust fluxes [e.g., *Zender et al.*, 2003; *Tegen et al.*, 2002] or compute dust emissions as function of surface wind speed, directly, rather than friction velocity, implicitly assuming constant surface roughness [e.g., *Ginoux et al.*, 2001]. This is due to the fact that until now, no global data set on surface roughness in arid regions existed. Typically, a low surface roughness on the order of 0.001 cm is used to describe active dust sources. In addition, land surface roughness plays a major role in atmosphere-surface interaction in general circulation models (GCM) and numerical weather prediction (NWP) schemes, through its impact on wind profile and flux transfer, especially in arid and semi-arid regions.

[3] However, very few estimates of the aerodynamic roughness length are available, despite the importance of this parameter. In situ measurements usually consist in measuring the wind velocity profile from several anemometers on a mast, in near-neutral stability conditions. This is

[1]Laboratoire d'Etudes du Rayonnement et de la Matière en Astrophysique, Observatoire de Paris, CNRS, Paris, France.
[2]Max-Planck-Institute for Biogeochemistry, Jena, Germany.
[3]Laboratoire de Météorologie Dynamique, École Polytechnique, CNRS/IPSL, Palaiseau, France.
[4]Laboratoire Interuniversitaire de Systèmes Atmosphériques, CNRS, Créteil, France.
[5]Centre d'étude des Environnements Terrestre et Planétaires, CNRS, Vélizy, France.

0148-0227/05/2004JD005370

not a parameter that is routinely measured in weather stations. *Greeley et al.* [1997] provided the largest set of quality measurements covering several sites. *Marticorena et al.* [1997] and *Callot et al.* [2000] developed maps of aerodynamic roughness length for North Africa and the Middle East, based on a geomorphological approach that combines topographic data, geological information, aerial pictures, and in situ observations. These maps are fixed in time and thus do not account for potential variation of the roughness length, related to vegetation cycle for instance or to anthropogenic impact. In GCM and NWP models, the aerodynamic roughness length is usually estimated from topographic maps in arid regions and from vegetation information elsewhere [*Sellers et al.*, 1997], with very large regional differences from a model to the other.

[4] Satellite observations appear to be the only realistic and effective solution for a global homogeneous and systematic monitoring of these arid regions. Radar observations are known to be sensitive to surface roughness, among other parameters. Pioneer work by *Greeley et al.* [1997] demonstrated a high correlation between z_0 and the radar backscattering σ_0 using observations from aircraft and from the Shuttle Radar Laboratory at 1.4 and 5.25 GHz in coincidence with field measurements. *Deroin et al.* [1997] characterized the soil roughness from the high spatial resolution synthetic aperture radar (SAR) at 5.3 GHz on board European Remote Sensing (ERS) satellite. More recently, *Zribi et al.* [2003] derived the rock fraction from ERS SAR measurements in two regions in Israel and Morocco. However, the large data volumes associated with these SAR observations as well as their very incomplete coverage on a global and continuous basis limit their use to local studies for a specific time.

[5] Recently, *Marticorena et al.* [2004] estimated the surface roughness over North Africa from measurements with the POLarization and Directionality of the Earth's Reflectance (POLDER) instrument on board ADEOS I. Given that the bidirectional reflectance in arid regions decreases with the shading effect of roughness elements like stones and pebbles, they derived an empirical relationship between the observed bidirectional reflectances and the roughness estimates from in situ measurements [*Greeley et al.*, 1997] and from the geomorphological maps [*Marticorena et al.*, 1997] and applied it to POLDER data over North Africa. A limitation of this method is essentially the high sensitivity of the observations to clouds as well as to aerosols in the atmospheric column. In addition, owing to a very limited acquisition period on both ADEOS 1 and 2, global maps for the various seasons cannot be estimated.

[6] On the basis of the observed relationship between the SAR radar observations and aerodynamic roughness, this study explores the potential of scatterometer observations for global continuous monitoring of the aerodynamic surface roughness. The SAR and the scatterometers are both active microwave instruments that measure the signal backscattered by the land surface. They are based on the same physics principles and actually, on the ERS satellite for instance, they share a large part of their hardware. Contrarily to the SAR, the ERS scatterometer provides a full coverage of the globe every ~4 days with a 50-km spatial resolution that is compatible with climatological application.

[7] The objective of this study is to derive a practical method to estimate the aerodynamic roughness length from ERS scatterometer observations over arid and semi-arid regions, on a global basis with a spatial resolution compatible with meteorological and climatological studies. The ERS scatterometer observations are presented in section 2. In section 3, a relationship is derived between the scatterometer observations and the aerodynamic roughness length, following a methodology similar to the one developed by *Marticorena et al.* [2004] using POLDER observations. Global results are presented in section 4 and are evaluated against existing land surface characterization. The satellite-derived roughness lengths are then evaluated in an aerosol transport model (section 5). Section 6 concludes this study.

2. ERS Microwave Backscattering at 5.25 GHz

[8] Active microwave observations over the entire globe are available since July 1991 with the launch of the ERS satellite carrying a wind scatterometer operating at 5.25 GHz. Although primarily designed for estimating wind speed and direction over the ocean, scatterometers have shown good correlations with land surface properties like vegetation density or soil moisture at global and regional scales [*Kerr and Magagi*, 1993; *Wismann et al.*, 1993; *Frison and Mougin*, 1996; *Wagner et al.*, 2003]. General characteristics and performances of the ERS scatterometer are summarized by *Frison and Mougin* [1996]. The backscattering signal is continuously measured by three antennas, one looking perpendicular to the satellite flight path and the other two pointing 45° forward and backward, respectively. The instrument scans a 500-km-wide swath with viewing angles ranging from 18° to 59°. The ERS scatterometer shares some hardware with the SAR, and the two are exclusive in their use. Therefore, over some areas where the SAR is typically on (North America and Europe), the temporal sampling rate for the scatterometer is lower. The scatterometer response is very stable over time for nonchanging targets, and the measurement uncertainty is estimated to be about 5%. Water vapor and cloud absorption and emission are negligible at 5.25 GHz, and no atmospheric correction is required. The antenna intercalibration is very good, which enables the use of all three antennas. For a given location, variation of the scattering signal with incidence angle is the dominant source of variability [*Messeh and Quegan*, 2000]. For all its incidence angles, scatterometer responses can be approximated by a linear function of the incidence angle.

[9] Following the method developed by *Frison and Mougin* [1996], for each cell on an equal-area grid, whose dimensions at the equator are 0.25° × 0.25°, a linear fit between the ERS σ_0 and the incident angle is calculated for a month and the fitted value at 45° is kept. Figure 1 shows the backscattering ERS coefficient σ_0 in dB versus the incidence angle, for three arid regions for July 1993, separating the measurements by antennas. For each area, the linear regression in θ is given. The first site is located in the Tassili-Ta-n Ahaggar in Algeria, the second in Death Valley in California, and the last one in the Oriental Grand Erg in Algeria. These three locations have been selected as representative of three typical situations. Other loca-

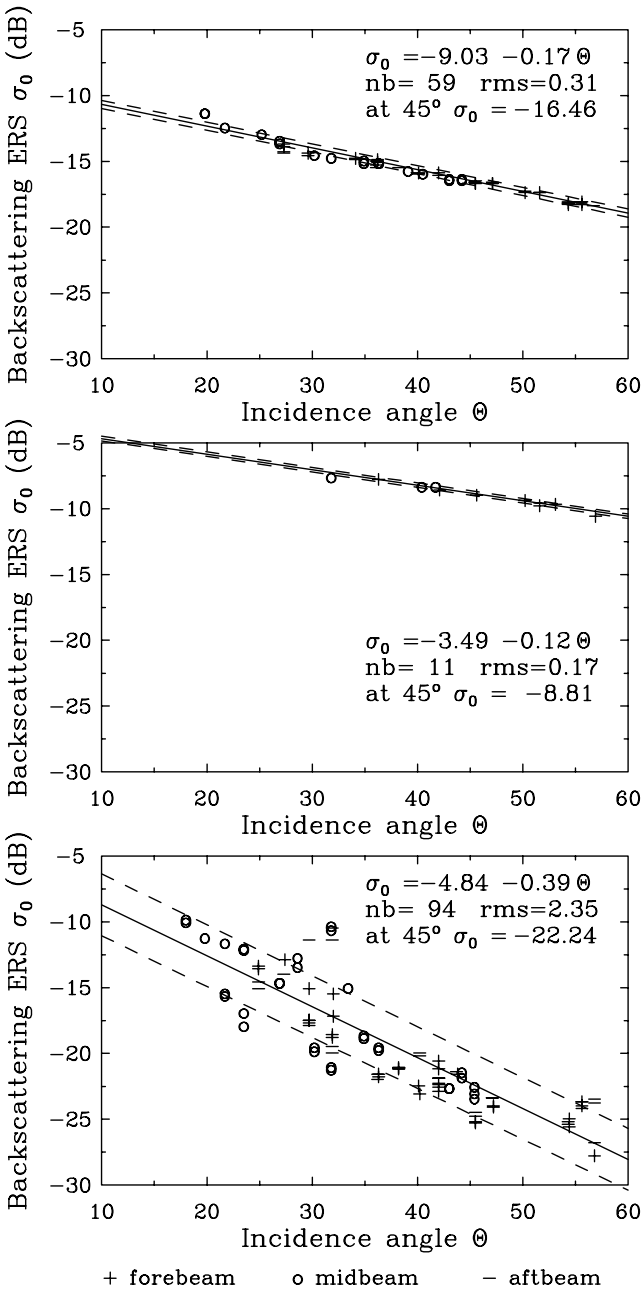

Figure 1. Backscattering ERS coefficient σ_0 in dB versus the incidence angle, for three arid regions for July 1993: (top) 21°40′N–4°20′E; 21°21′N–4°48′E (Tassali-Ta-n Ahaggar in Algeria), (middle) 36°08′N–116°42′W; 36°25′N–116°54′W (Death Valley in California), and (bottom) 31°39′N–8°34′E; 31°13′N–9°03E (Oriental Grand Erg in Algeria). For each area, the linear regression in θ is given (solid line), along with the number of pixels considered, the root-mean-square (rms) of the linear fit, and the value of the fit at 45° incidence. The dashed lines indicate the linear fit plus and minus 1 rms deviation.

tions with similar physical characteristics show similar scatterometer responses. The last case (Figure 1, bottom) corresponds to an area of sand dunes where radar volume scattering takes place in addition to the surface scattering. As a consequence, more variability in observed in the measurements. Figure 2 presents the global map of the backscattering coefficient interpolated at 45°, averaged over a year (1993). The equatorial forests are associated with large σ_0 due to volume scattering in the vegetation. Large-scale surface roughness caused by topography (e.g., the Himalayas) also increases significantly the backscattering signal at 45°. Arid regions are characterized by low σ_0, the lowest values being encountered in sand deserts because of the combined effects of low surface roughness and wave penetration.

3. Relationship Between the Surface Roughness and the Scatterometer Backscattering: A Practical Solution

[10] An extensive body of research has been directed toward a better understanding of the mechanisms responsible for the backscattering of bare soil, both from theoretical analysis and from small-scale field experiments. Bare soil response depends on surface roughness and soil dielectric properties. Smooth bare soils have a close-to-specular reflection (i.e., it nearly obeys the Snell/Descartes Law), producing low backscattering coefficient when observed off-nadir. When the terrain gets rougher, surface scattering causes the backscattering coefficient off-nadir to increase. Physically based scattering models have been developed to predict the σ_0 as a function of surface characteristics, from simple parameterized models to more complex integral electromagnetic methods (IEM) [*Fung et al.*, 1992]. On the basis of IEM simulations, Figure 3 illustrates clearly the increase of backscattering radar coefficient with surface roughness, except for very small incident angles (lower than the scatterometer angles). Good agreement has been obtained between simulations and measurements on artificial rough surfaces [*Marcelloni et al.*, 2000]. In addition, in very dry terrain like sand desert, the radar signal can significantly penetrate the surface involving volume scattering and thus a decrease of the backscattering coefficient. Even though the gross behavior of the real surface observations can usually be interpreted by simulations, it is difficult to have satisfactory agreement between the real observations and simulations, even during well-controlled small-scale experiments [*Zribi et al.*, 1997]. The major problems are expected to arise from (1) the difficulty of a model to account for all the backscattering interactions with the scattering surface and potentially its subsurface and (2) the difficulty to describe the real surface characteristics, especially its roughness [*Davidson et al.*, 2000]. The characterization of surface roughness for radar modeling is generally based on measurements made by pin profiler or laser profilers. The surface roughness height is considered to be a stochastic system. The properties of ergodicity and stationarity are assumed in order to deduce different statistical parameters from calculated height correlation function on the profile, like the root mean square height and the correlation length. These parameters are generally not very stable, in particular the correlation length estimation. Furthermore, the height correlation function shape has a large impact on the backscattering levels simulated with the model although Gaussian or exponential shapes are generally used to simplify the analytical computations, thus restricting the accuracy of the surface description. On

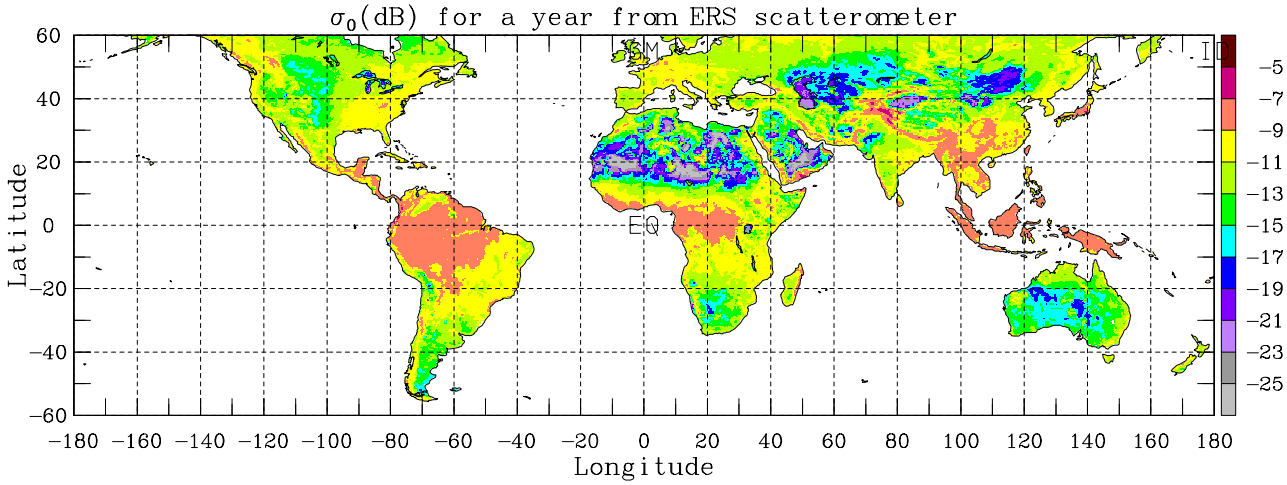

Figure 2. Global map of a yearly mean backscattering ERS coefficient σ_0 (as interpolated at 45°).

the basis of these estimated statistical parameters and additional information such as the dielectric properties of the media, backscattering coefficient can theoretically be derived, but the mentioned difficulties make this approach very difficult to develop, especially on a global scale.

[11] Our objective is to find a practical relationship between the aerodynamic roughness length and the ERS σ_0, on a global basis and at a regional scale (0.25° × 0.25°). At this scale and over such a variability of surfaces, inverting the roughness length from a scattering model would be very difficult and questionable. The lack of major model parameters like the dielectric properties at a global scale would be one of several problems. Instead, a direct statistical relationship is established between the available reliable roughness length estimates and the backscattering coefficients. The derived roughness maps will be evaluated against other sources to test a posteriori the pertinence of the approach.

[12] The quality measurements provided by *Greeley et al.* [1997] in California, Nevada, and Namibia are used, in addition to the geomorphological estimates from *Marticorena et al.* [1997] and *Callot et al.* [2000] that cover North Africa and the Middle East. Homogeneous regions have been carefully selected from the geomorphological estimates [*Marticorena et al.*, 2004] for comparison with large-scale satellite observations. Table 1 summarizes the regions chosen for the comparison and indicates the measurement sources. Figure 4 shows the relationship between z_0 and the ERS σ_0, for both *Callot et al.* [2000] estimates and *Greeley et al.* [1997] in situ measurements. A log linear relationship is deduced between σ_0 and z_0 in arid areas. The monthly mean standard deviation on each σ_0 estimates are taken into account (see Table 1). In the regression, 79% of the variance is explained by this log linear relationship. The associated errors in z_0 vary with σ_0: A slight increase of the uncertainty can be noticed for

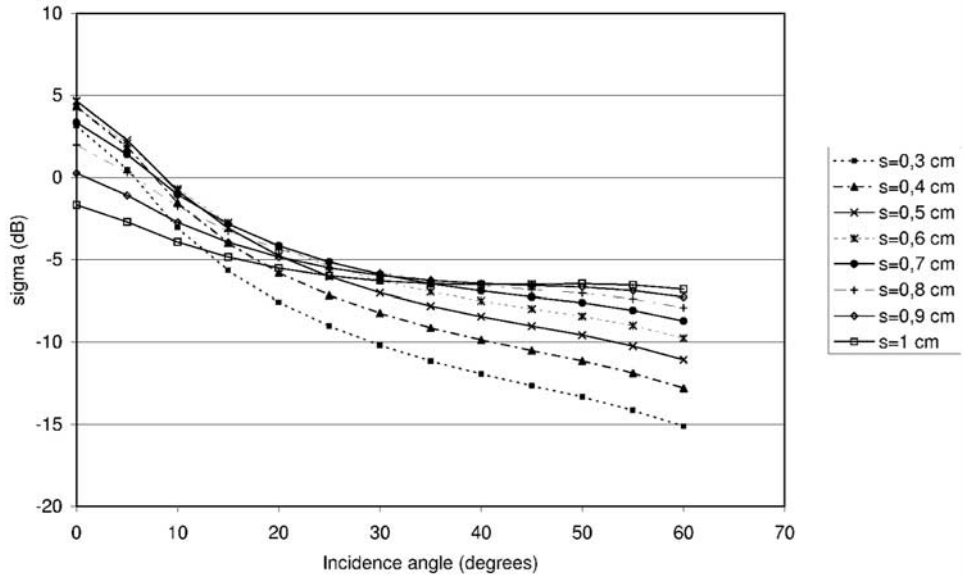

Figure 3. Integral electromagnetic methods (IEM) backscattering simulations as a function of incidence angles for different surface roughness (with rms ranging from 0.3 to 1 cm).

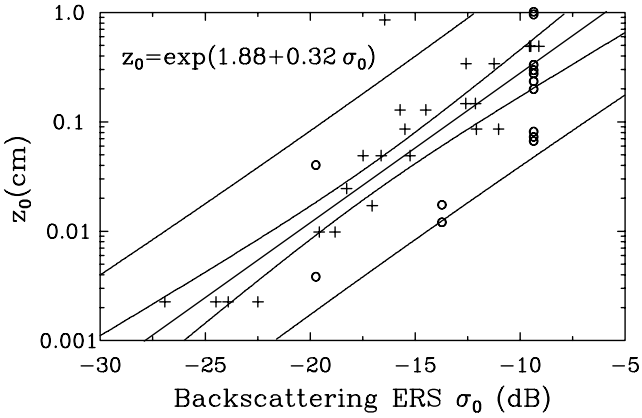

Figure 4. Scatterplot of the selected z_0 estimates from *Marticorena et al.* [1997] and *Callot et al.* [2000] (pluses) and from *Greeley et al.* [1997] (circles) versus the backscattering ERS coefficient σ_0 for the corresponding areas. The log linear regression is indicated by a solid line, and the dashed lines represent the 95% confidence interval and the 2 standard deviation interval (respectively, close and farther from the linear regression).

low and high values of σ_0. This is expected since this is where the dispersion in the data is higher. It has been checked (not shown) that the regression is very robust and does not change significantly when suppressing these values. This regression being only based on z_0 estimates in arid and semi-arid regions, it will only be applied to arid areas where σ_0 values are low, thus excluding densely vegetated regions with large σ_0.

4. Global Results and Evaluation of the Estimated Aerodynamic Roughness Length

[13] The log linear relation previously derived is applied to the monthly mean ERS σ_0 to derive monthly mean z_0 all over the globe. Figure 5 presents the annual mean z_0. Only low z_0 values are presented. The parameterized approach has been developed for arid soil and cannot be directly applied to other areas. All major deserts appear on this map. The sand deserts are associated with z_0 below ~0.02 cm. As expected, they cover large areas in North Africa and in Arabia, and are also present in Asia (e.g., Taklamakan and Gobi deserts). These regions also correspond to the major mineral aerosol sources.

Table 1. Regions Used for the Aerodynamic Roughness Length Estimates With the Associated ERS σ_0 Mean Values and Standard Deviations for July 1993[a]

Regions		z_0, cm	Source	Mean σ_0, dB	Standard σ_0, dB
20°44′N 9°44′W	20°18′N 9°18′W	2.30E-3	M97	−26.92	2.78
31°36′N 7°00′E	31°14′N 7°25′E	2.30E-3	M97	−23.91	2.19
21°48′N 7°42′W	21°20′N 7°15′W	2.30E-3	M97	−24.49	2.76
31°39′N 8°34′E	31°13′N 9°03′E	2.30E-3	M97	−22.49	2.47
23°42′N 0°59′E	23°18′N 1°22′E	1.00E-2	M97	−19.57	1.04
26°12′N 7°48′W	25°48′N 7°18′W	2.50E-2	M97	−18.27	0.68
21°42′N 5°20′E	21°15′N 5°48′E	5.00E-2	M97	−17.48	0.60
21°40′N 4°20′E	21°21′N 4°48′E	5.00E-2	M97	−16.62	0.30
30°42′N 11°09′E	30°15′N 11°12′E	1.50E-1	M97	−12.59	0.59
30°10′N 10°45′E	29°45′N 11°12′E	1.50E-1	M97	−12.13	0.67
25°42′N 8°10′E	25°18′N 8°32′E	5.00E-1	M97	−9.50	0.57
33°36′N 1°18′W	33°12′N 0°48′W	8.73E-1	M97	−16.45	0.98
26°42′N 4°54′W	26°18′N 4°27′W	5.00E-2	M97	−15.25	0.54
25°42′N 8°10′E	25°16′N 8°37′E	5.00E-1	M97	−9.56	0.58
26°12′N 8°17′E	25°46′N 8°32′E	5.00E-1	M97	−9.11	0.92
33°28′N 2°53′E	33°12′N 3°30′E	3.47E-1	M97	−12.58	0.80
33°37′N 3°31′E	33°12′N 4°01′E	3.47E-1	M97	−11.24	0.78
26°59′N 3°44′W	26°46′N 3°09′W	1.31E-1	M97	−15.72	0.90
27°47′N 8°43′W	27°28′N 8°17′W	1.31E-1	M97	−14.50	0.97
26°41′N 2°00′E	28°09′N 2°24′E	8.73E-2	M97	−15.49	2.41
28°41′N 2°40′E	28°09′N 2°55′E	8.73E-2	M97	−11.03	1.64
29°46′N 2°58′E	29°14′N 3°35′E	8.73E-2	M97	−12.08	0.78
23°50′N 7°82′W	23°27′N 7°37′W	1.74E-2	M97	−17.05	1.15
22°30′N 0°53′E	22°17′N 0°37′E	1.00E-2	M97	−18.82	0.75
23°36′S 14°56′E	23°24′S 14°44′E	4.00E-3	G97	−19.73	1.71
23°36′S 14°56′E	23°24′S 14°44′E	4.00E-2	G97	−19.73	1.71
36°26′N 116.54°56′W	36°14′N 116°42′W	1.00E-0	G97	−9.36	0.48
36°26′N 116.54°56′W	36°14′N 116°42′W	2.45E-1	G97	−9.36	0.48
36°26′N 116.54°56′W	36°14′N 116°42′W	1.06E-0	G97	−9.36	0.48
36°26′N 116.54°56′W	36°14′N 116°42′W	8.50E-2	G97	−9.36	0.48
36°26′N 116.54°56′W	36°14′N 116°42′W	6.96E-2	G97	−9.36	0.48
36°26′N 116.54°56′W	36°14′N 116°42′W	7.60E-2	G97	−9.36	0.48
36°26′N 116.54°56′W	36°14′N 116°42′W	3.10E-1	G97	−9.36	0.48
36°26′N 116.54°56′W	36°14′N 116°42′W	2.88E-1	G97	−9.36	0.48
36°26′N 116.54°56′W	36°14′N 116°42′W	2.08E-1	G97	−9.36	0.48
36°26′N 116.54°56′W	36°14′N 116°42′W	3.47E-1	G97	−9.36	0.48
38°23′N 116°00′W	38°08′N 116°15′W	1.82E-2	G97	−13.73	0.55
38°23′N 116°00′W	38°08′N 116°15′W	1.26E-2	G97	−13.73	0.55

[a]M97, *Marticorena et al.* [1997]; G97, *Greeley et al.* [1997]. Read 2.30E-3 as 2.30×10^{-3}.

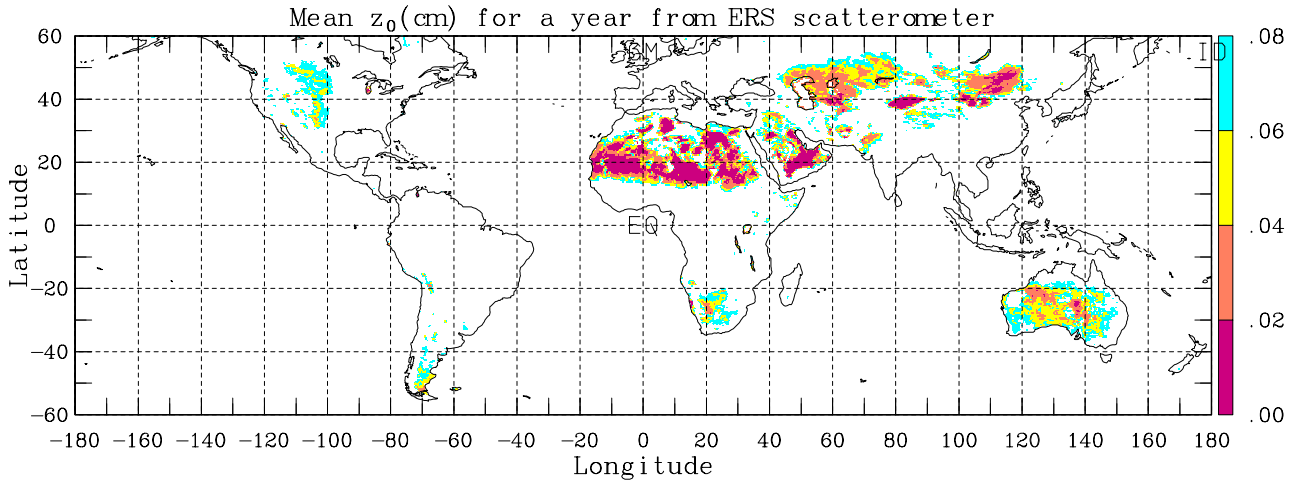

Figure 5. Global map of a year mean z_0 estimated from the backscattering ERS coefficient σ_0. Values over 0.08 cm have been omitted.

[14] The higher roughness lengths retrieved for the arid and semi-arid regions in North and South America, southern Africa, and Australia, as well as in large parts of Central Asia, are consistent with the view that those areas are only emitting small amounts of dust under current climate conditions. For Australia, low surface roughness values below 0.02 cm only occur near the Lake Eyre basin, the area of highest dust emissions on the Australian continent [e.g., *Hesse and McTainsh*, 2003]. Many (not all) of the regions with low surface roughness shown in Figure 5 coincide with regions where dust hot spots are observed in the total Ozone Mapping Spectrometer Absorbing Aerosol Index (TOMS AI) [*Herman et al.*, 1997]. That is the case for, for example, the Taklamakan desert in China, the Lake Eyre Basin in Australia, and the Bodele and Chott Djerid areas in the Sahara. Those areas have been associated with enclosed topographic depressions, where fine sediment could have accumulated [*Prospero et al.*, 2002]. Such depressions could have been lakes during former wet climate periods, allowing accumulation of sediments. For those regions it can be expected that the surface is relatively smooth, with low roughness parameters. Other regions for which high dust storm frequencies have been observed [*Middleton*, 1989] can be identified on the map: the Gobi desert in China, the Karakum desert in Turkmenistan, the region surrounding the Aral Sea, and the Thar desert in India. Smaller and less documented deserts such as the desert valleys of the Baloutshistan region in Pakistan or the Lut desert in Iran also appear clearly.

4.1. Comparison With the Geomorphologic Estimates and With the Surface Soil Characteristics From the FAO

[15] Geomorphological estimates of the aerodynamic roughness length [*Marticorena et al.*, 1997; *Callot et al.*, 2000] are available for North Africa and the Middle East, between 15°N and 35°N and between −20°W and 80°E. For each square degree in this region, Figure 6 (top) represents the aerodynamic roughness length associated to the dominant surface type. Figure 6 (middle) shows the geographical extent of sand dunes, as characterized by *Food and Agriculture Organization* (*FAO*) [1977] classification, for the same region but limited to 60°E. The aerodynamic roughness length estimated from ERS is presented in Figure 6 (bottom) for the same region. The FAO sand deserts generally coincide with areas of low z_0 (less than 0.02 cm), although the extent of the regions might differ and significant differences can exist in some locations. In fact, the FAO sand desert classification corresponds to the main sand seas: the Great Eastern and Western Erg south of Algeria and Morocco, the Lybian sand sea, the Rub Al Khali sand sea in the Arabian peninsula, the sand seas extending from Mauritania to the north of Mali and north of Niger and Chad surrounding the Bodele depression. The locations of these sand seas are consistent on the three maps, most discrepancies being located around the main sand desert structures. Figure 7 outlines the spatial structure differences between the FAO classifications and the regions with z_0 below 0.01 cm. Such differences can be largely related to differences in the spatial resolutions ($1° \times 1°$ as compared to $0.25° \times 0.25°$). In addition, the FAO map only shows purely sandy surfaces, while low z_0 appears on the [*Marticorena et al.*, 1997; *Callot et al.*, 2000] map only if it corresponds to the dominant soil type. The ERS map describes the smooth surfaces with a high spatial resolution ($0.25° \times 0.25°$). This also explained the fact that small smooth surfaces are observed both on the ERS map and on the *Marticorena et al.* [1997] and *Callot et al.* [2000] map, such as the sandy surfaces in the northwestern coast of the Persian Gulf and the Lut and Baloutshistan deserts or the sandy surfaces along the Mauritanian coast. Small but noticeable differences between these two maps appear in the Middle East and Minor Asia. The salty desert of Dasht-e Kevir does not appear as a smooth surface on the ERS map, maybe because of specific properties of salty soils. Conversely, the Thar desert has a smaller extent in the *Marticorena et al.* [1997] and *Callot et al.* [2000] map than in the ERS maps: This may be due to the temporal variability of the vegetation cover in this area that is not taken into account in the geomorphologic estimate.

[16] For a more quantitative comparison, Figure 8 (top) shows the normalized histograms of the z_0 estimated from

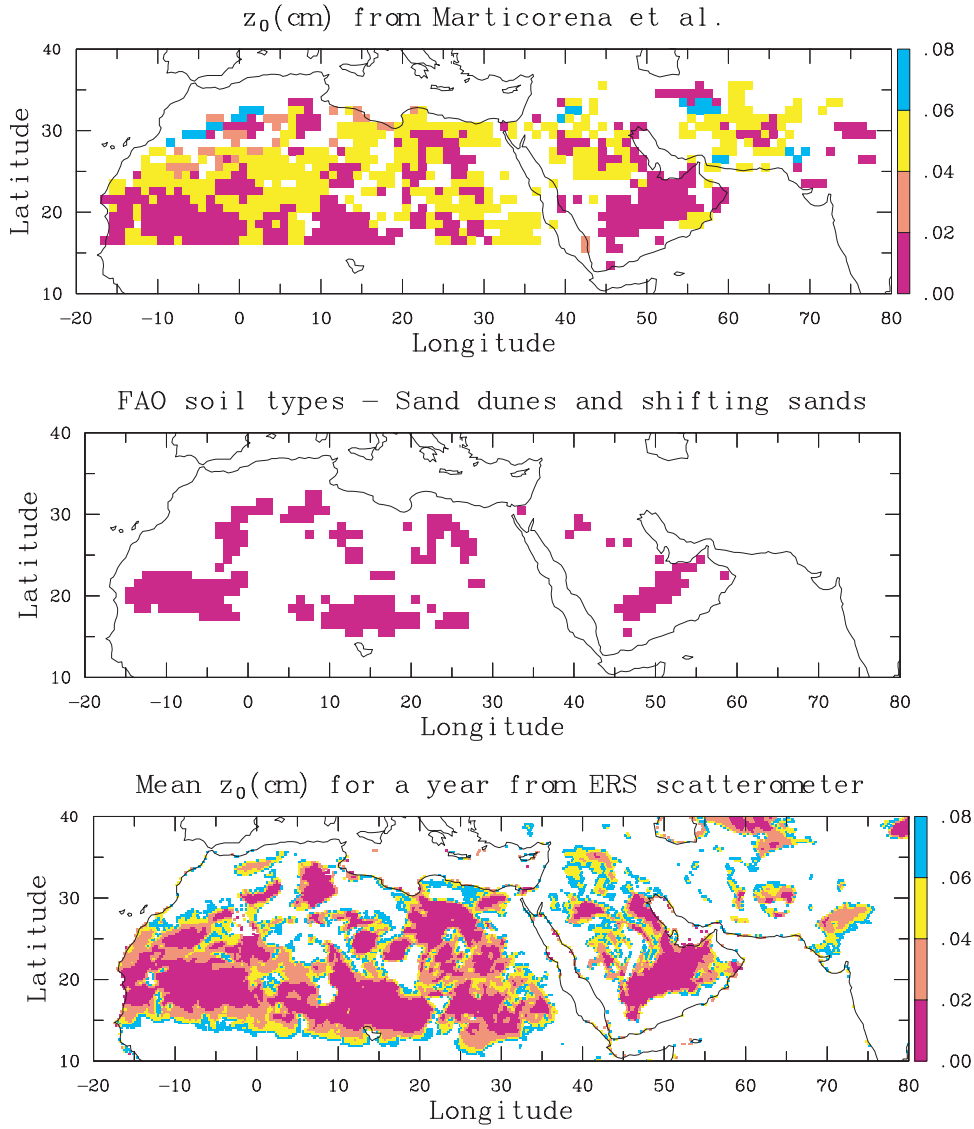

Figure 6. (top) The aerodynamic roughness length associated to the dominant surface type from *Marticorena et al.* [1997] and *Callot et al.* [2000]. (middle) The sand deserts in North Africa, as characterized by the *FAO* [1977] classification. (bottom) The mean aerodynamic roughness length estimated from ERS for 1993.

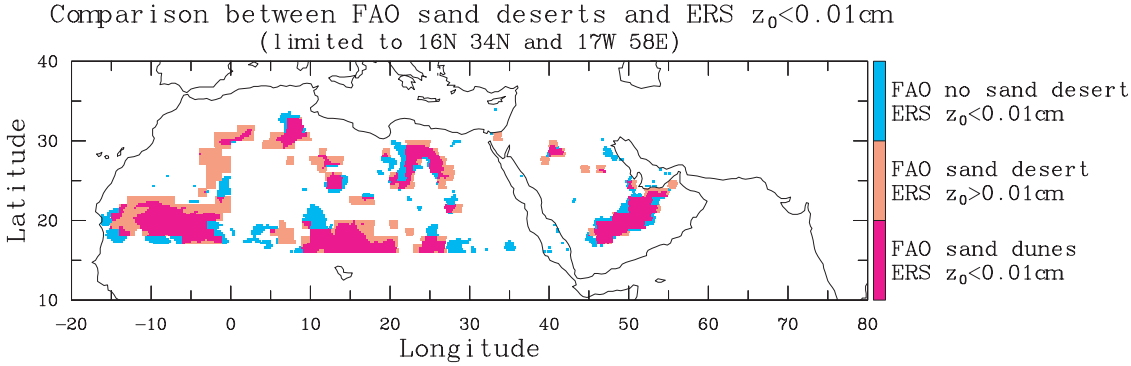

Figure 7. Correspondences between the sand deserts from the *FAO* [1977] classification and the ERS z_0.

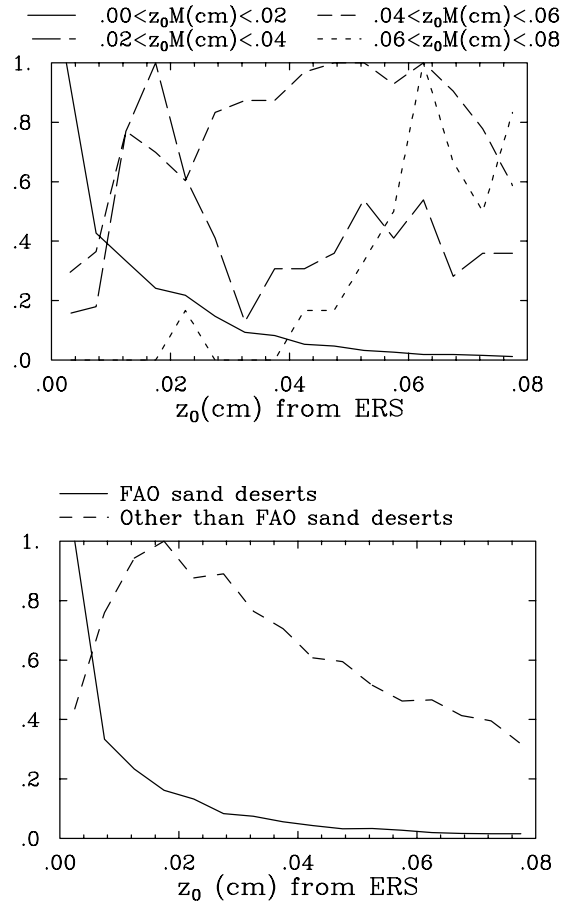

Figure 8. (top) The normalized histograms of the z_0 estimated from ERS, for four classes of z_0 as derived from *Marticorena et al.* [1997]. (bottom) Same as above but with the *FAO* [1977] classification.

ERS, for four classes of z_0 as derived from *Marticorena et al.* [1997]. The four histograms are rather well separated. However, for the lower ranges of Marticorena et al. z_0 (below 0.04 cm), the scatterometer tends to produce lower values. The regions with very low z_0 in the Marticorena et al. classification generally correspond to sand deserts. In this very dry sand, volume scattering of the microwave radiation will take place that can significantly decrease the radar backscattering coefficient. Figure 8 (bottom) shows similar histograms, but for the FAO classification. The sand desert and the rest of the arid regions are clearly well separated by the ERS z_0 estimates.

4.2. Seasonal Variation of z_0 Satellite Estimates

[17] Current z_0 estimates are fixed in time, although seasonal variations are expected, especially in semi-arid regions where sparse vegetation can appear during the year. The ERS backscattering coefficients are sensitive to the presence of vegetation, as well as to changes in soil moisture. Vegetation acts as volume scatterer, and vegetation density increases the backscattering coefficient for off-nadir observations. Soil moisture also increases σ_0. Figure 9 shows the variability of the monthly mean z_0 for a year, as estimated from ERS scatterometer. The regions with the largest z_0 variations are located in the Sahelian transition zone where the vegetation undergoes a marked seasonal cycle. For a region east of Lake Chad, Figure 10 presents the seasonal cycle of the ERS σ_0 and derived z_0, along with the AVHRR NDVI information, every other month during a year. After the rainy season, the vegetation increase (see the NDVI increase in September) is clearly associated with an increase in the z_0, as expected.

5. Implementing ERS Derived z_0 Into a Global Model of the Dust Cycle

[18] The satellite-derived surface roughness parameters were implemented into the dust emission scheme of the global dust cycle model described by *Tegen et al.* [2002]. Computation of dust fluxes is based on the scheme developed by *Marticorena et al.* [1997]. This scheme explicitly takes into account the dependence of dust emissions upon surface wind speeds, surface roughness, soil particle size distribution, soil moisture, and snow cover. It includes a dependence of dust emissions on monthly vegetation cover and type, and topographic depressions are considered as preferential areas of dust emission. Dust emissions are computed on a 0.5° grid, using ECMWF T106 15-year reanalysis (ERA15) 10-m wind velocity fields on 6-hourly time steps. In the emission computation, the surface roughness z_0 is used to compute the friction velocity from the 10-m surface wind speed, and to modify the threshold velocity that must be reached to initiate dust emission. Originally, the surface roughness parameter was set to a globally constant low value of z_0 = 0.001 cm in active dust source areas. We replaced this constant value with the satellite-derived z_0 which varies at each grid cell. Because the satellite z_0 are generally higher than the originally used constant value, dust emissions were suppressed in many regions when using the standard model parameterization. The dust emission model had been previously tuned to match the satellite-observed dust event frequency and fluxes, using the constant z_0. Further calibration of the model parameterization is to be expected when using a new source of information. We thus lowered the threshold wind friction velocity that must be reached to initiate dust emission by 25% in each grid cell. This led to global annual dust emissions of 1510 Mt/yr for the 1983–1992 average. This is comparable to the dust emissions of 1740 Mt/yr for the same period, which were computed using constant low roughness lengths [*Tegen et al.*, 2004]. The resulting regional distributions of annual emission fluxes for 10-year averages derived from constant and varying z_0, respectively, are markedly different in the Sahara, while differences are relatively small in Asian and Australian deserts (Figure 11). Many areas that show small dust emission, for example, in central Asia and North America in the experiments using constant z_0, have zero dust fluxes when using a spatially varying z_0. In source regions, dust may be emitted from small preferential sources like dried lake beds; it could be argued that the scale of the satellite-derived z_0 could be too coarse compared to the scale of the emission hot spots. In the emission model we prescribe the fraction of a model grid cell covered by a potential maximum extent of dried lake beds as preferential sources for dust

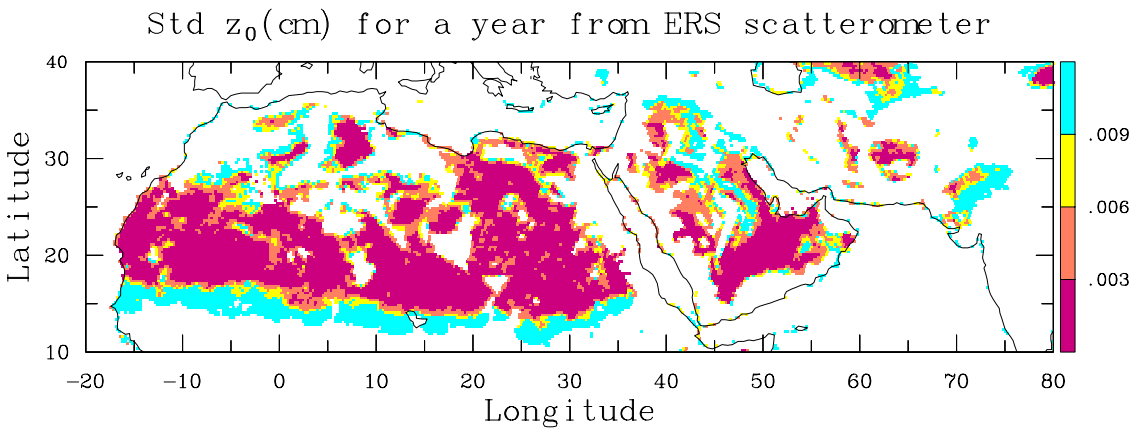

Figure 9. Standard deviation of the ERS z_0 calculated for 1993 over Africa and Middle East.

emission. With this parameterization, 28.5% of the preferential source area covers at least one 0.5° grid cell, 61% of the preferential sources areas cover at least half of a 0.5° grid cell. When computing the actual dust emissions from these preferential "hot spot" areas, we find that 41% of dust particles with less than 10μm radius are emitted from hot spots that completely cover the half-degree grid cell, 72% are emitted from preferential sources that cover at least half of the grid cell. This indicates that the major part of dust emissions from the preferential sources (as parameterized in the emission model) occurs on spatial scales that are comparable to the satellite surface roughness product. However, there are still remaining uncertainties, as the actual hot spots may be smaller than the maximum "potential dry lakes" that we have prescribed in the emission model.

[19] Validating dust emission fluxes directly is not straightforward, as measurable dust indicators (e.g., dust concentration measurements at surface stations) record not only variations in dust emissions, but are strongly influenced by transport direction and deposition. The TOMS AI, which is available with daily global coverage since 1979, has frequently been used to investigate dust aerosol distributions [e.g., *Ginoux and Torres*, 2003] with the caveat that the retrievals depend on the height of the aerosol layer and that black carbon aerosols from biomass and industrial burning also contribute to the AI signal in addition to the absorbing dust aerosols. The frequency of observation of high TOMS AI events has been used to characterize strong dust source areas [*Prospero et al.*, 2002; *Mahowald and Dufresne*, 2004]. We compare the North African and Arabic peninsula number of dust events with observed frequencies of days when TOMS AI is larger than 2.5 and 1 for July 1987 when both biomass burning emissions and the influence of boundary layer height variations on the AI retrieval are small [*Mahowald and Dufresne*, 2004] (Figure 12). This threshold of AI 2.5 was chosen to result in similar numbers of dust events in the model and TOMS AI events. We find that the number of dust events using spatially varying z_0 (Figure 12b) are enhanced in the Bodele region and significantly decreased west of Libya: This is consistent with the frequency of TOMS AI observations larger than 1 or 2.5 (Figures 12c and 12d). The mountain range west of Saudi Arabia that is erroneously associated with a high number of dust events when using the fixed z_0 value does not appear as

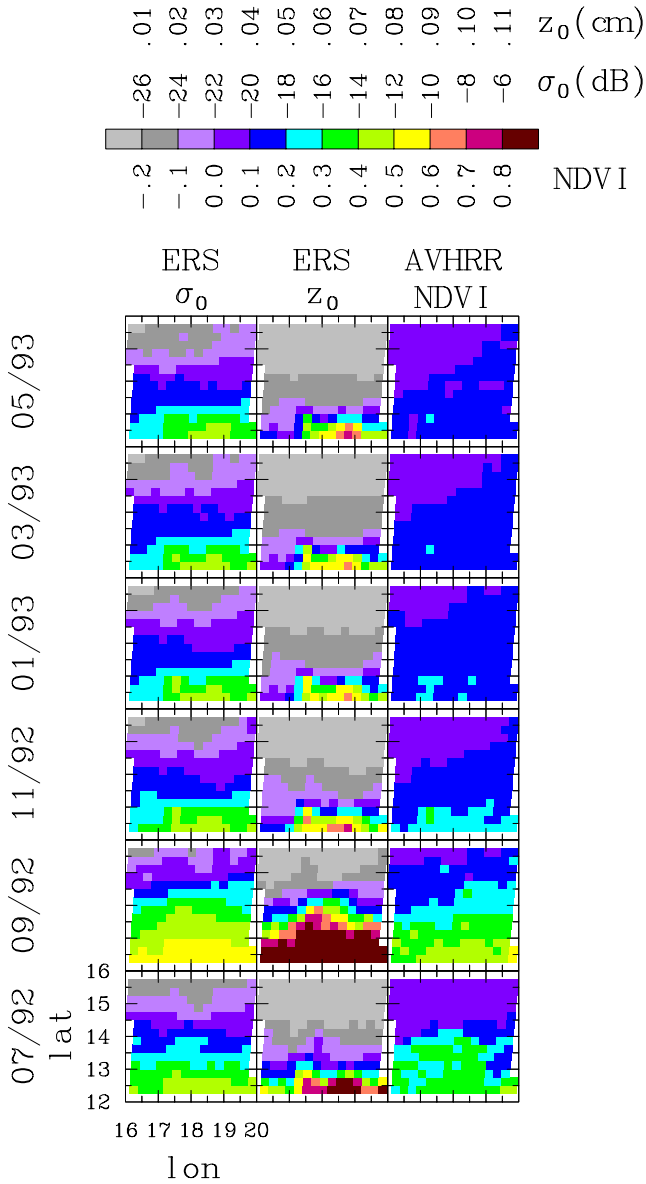

Figure 10. ERS σ_0, ERS z_0, and the AVHRR NDVI for every other month between July 1992 and June 1993, for an area in Chad.

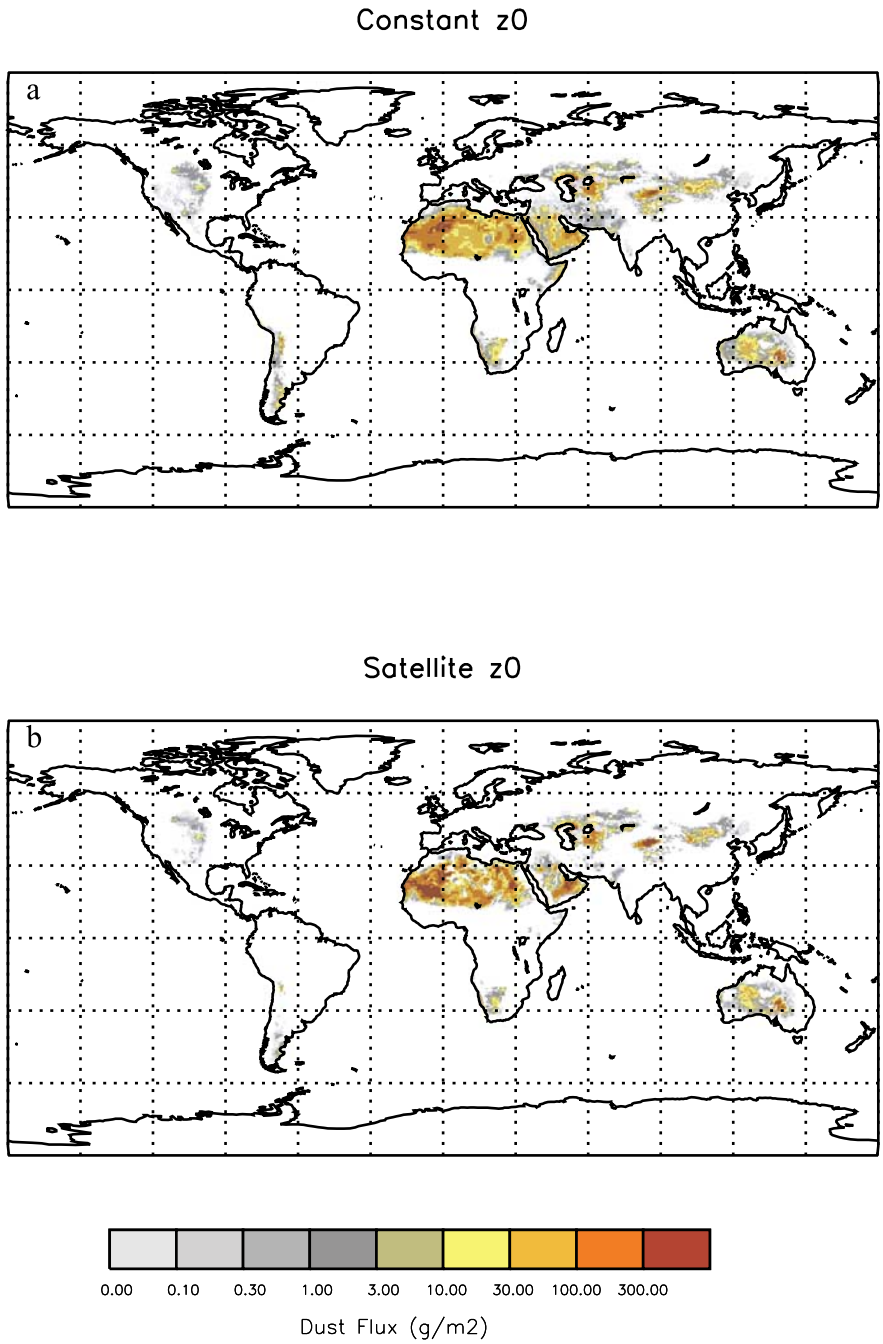

Figure 11. Comparison of dust emissions (a) computed with a constant $z_0 = 0.001$ cm and (b) computed with the ERS satellite derived spatially varying z_0. The emissions are computed with the model of *Tegen et al.* [2004]. The annual average emissions are shown for 1983–1992.

a significant source of dust with the satellite-derived z_0, as expected. In addition, the maximum number of Sahara dust emission events is shifted southward when using the spatially varying z_0. Qualitatively, this agrees better with the TOMS observation frequencies for these regions (Figures 12c and 12d). This is an indication that global-scale dust emission computations are improved when including spatially varying z_0 as input parameter. The spatial correlation between the TOMS observation frequency and the modeled dust events increases from 0.34 when using the fixed z_0 to 0.52 when using the varying satellite z_0: This is a clear improvement that shows the benefit of the global satellite estimates. For a more quantitative analysis, dust emission fluxes should be included into a tracer model that simulates the atmospheric dust distribution from emission, transport, and deposition. Then, computed dust distributions can be compared directly with measured aerosol optical thicknesses, AI, and surface concentration. This will be the object of a future study.

6. Conclusions

[20] Estimates of the aerodynamic roughness lengths in arid and semi-arid regions are for the first time provided for

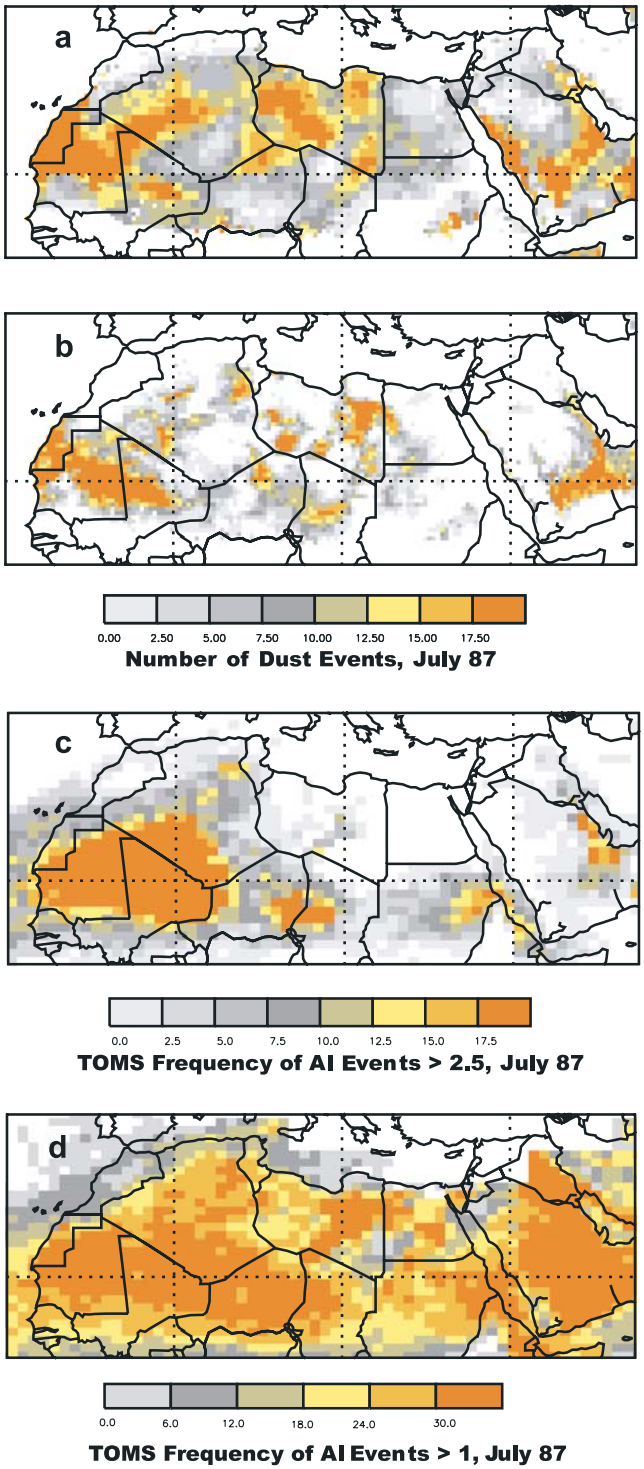

Figure 12. Frequency of dust events from North Africa and the Arabic peninsula (July 1987) (a) for the dust emission model using constant z_0 and (b) for the spatially varying satellite-derived z_0, as compared to the frequency of observed events of TOMS AI (c) above 2.5 and (d) above 1 for the same month.

the whole globe, using satellite ERS scatterometer observations. A parameterization is derived between the ERS scatterometer backscattering coefficients and quality in situ and geomorphological z_0 estimates. It is a practical solution to provide realistic roughness lengths that have consistent spatial patterns and can provide reasonable temporal variations. The ERS derived z_0 estimates show large-scale spatial patterns that are consistent with independent surface characterization. In addition, they correctly reproduce the expected vegetation -related z_0 changes in semi-arid regions. The analysis can easily be revisited to account for additional in situ or other z_0 estimates that would become available. Monthly mean global z_0 maps for several years are available to the community.

[21] We showed a qualitative indication that dust emission computations are improved when using the ERS derived z_0 as input parameter. Because simulated dust emissions can only be validated indirectly, it is important to compute the full aerosol cycle, including dust transport and deposition. Measurements of dust concentration at remote surface stations and satellite-derived dust properties can then be used directly to validate the model results and test to what extent the inclusion of the spatially varying z_0 derived from the ERS satellite improves the model results.

[22] **Acknowledgments.** We would like to thank Gladys Gane for her help in processing the data during her stay at Paris Observatory. We are very grateful to Ron Miller for his careful reading of the text and a very constructive review. The ERS scatterometer data have been provided by IFREMER.

References

Alfaro, S. C., and L. Gomes (2001), Modeling mineral aerosol production by wind erosion: Emission intensities and aerosol distributions in source areas, *J. Geophys. Res.*, *106*, 18,075–18,084.

Callot, Y., B. Marticorena, and G. Bergametti (2000), Geomorphological approach for modeling the surface features over arid environments in a model of dust emission: Application to the Sahara desert, *Geodyn. Acta*, *13*, 245–270.

Davidson, M. W. J., T. Le Toan, F. Mattia, G. Satalino, T. Mannimen, and M. Borgeaud (2000), On the characterization of agricultural soil roughness for radar remote sensing studies, *IEEE Trans. Geosci. Remote Sens.*, *38*, 630–640.

Deroin, J. P., A. Company, and A. Simonin (1997), An empirical model for interpreting the relationship between backscattering and arid land surface roughness as seen with SAR, *IEEE Trans. Geosci. Remote Sens.*, *35*, 86–92.

Food and Agriculture Organization (FAO) (1977), Soil map of the world, 1:5M scale, U.N. Educ., Sci., and Cult. Org., Paris.

Frison, P.-L., and E. Mougin (1996), Use of ERS-1 wind scatterometer data over land surfaces, *IEEE Trans. Geosci. Remote Sens.*, *34*, 550–560.

Fung, A. K., Z. Li, and K. S. Chen (1992), Backscattering from a randomly rough dielectric surface, *IEEE Trans. Geosci. Remote Sens.*, *30*, 356–369.

Gillette, D. A., and R. Passi (1988), Modeling dust emission caused by wind erosion, *J. Geophys. Res.*, *93*, 14,233–14,242.

Ginoux, P., and O. Torres (2003), Empirical TOMS index for dust aerosol: Applications to model validation and source characterization, *J. Geophys. Res.*, *108*(D17), 4534, doi:10.1029/2003JD003470.

Ginoux, P., M. Chin, I. Tegen, J. Prospero, B. Holben, O. Dubovik, and S.-J. Lin (2001), Sources and distributions of dust aerosols simulated with the GOCART model, *J. Geophys. Res.*, *106*, 20,255–20,273.

Greeley, R., D. G. Blumberg, J. F. McHone, A. Dobrovolskis, J. D. Iversen, N. Lancaster, K. R. Rasmussen, S. D. Wall, and B. R. White (1997), Applications of space borne radar laboratory data to the study of aeolian processes, *J. Geophys. Res.*, *102*, 10,971–10,983.

Herman, J. R., P. K. Bhartia, O. Torres, C. Hsu, C. Seftor, and E. Celarier (1997), Global distribution of UV-absorbing aerosols from Nimbus 7/TOMS data, *J. Geophys. Res.*, *102*, 16,911–16,922.

Hesse, P. P., and G. H. McTainsh (2003), Australian dust deposits: Modern processes and the Quaternary record, *Quat. Sci. Rev.*, *22*, 2007–2035.

Intergovernmental Panel on Climate Change (1995), A report of the Intergovernmental Panel on Climate Change, 64 pp., Geneva.

Intergovernmental Panel on Climate Change (2001), *Climate Change 2001: The Scientific Basis, Third Assessment Report of the Intergovernmental*

Panel on Climate Change (*IPCC*), edited by J. T. Houghton et al., 944 pp., Cambridge Univ. Press, New York.

Joussaume, S. (1990), Three-dimensional simulations of the atmospheric cycle of desert dust particles using a general circulation model, *J. Geophys. Res.*, *95*, 1909–1941.

Kerr, Y. H., and R. Magagi (1993), Use of the ERS-1 wind-scatterometer data over land surfaces: Arid and semi-arid lands, paper presented at 2nd ERS-1 Symposium, Eur. Space Agency, Hamburg, Germany.

Mahowald, N. M., and J. L. Dufresne (2004), Sensitivity of TOMS aerosol index to boundary layer height: Implications for detection of mineral aerosol sources, *Geophys. Res. Lett.*, *31*, L03103, doi:10.1029/2003GL018865.

Marcelloni, G., G. Nesti, P. Pampaloni, S. Sigismondi, D. Tarchi, and S. Lolli (2000), Experimental validation of surface scattering and emission models, *IEEE Trans. Geosci. Remote Sens.*, *38*, 459–469.

Marticorena, B., and G. Bergametti (1995), Modeling the atmospheric dust cycle: 1. Design of a soil-derived dust production scheme, *J. Geophys. Res.*, *100*, 16,415–16,430.

Marticorena, B., G. Bergametti, B. Aumont, Y. Callot, C. N'Doumi, and M. Legrand (1997), Modeling the atmospheric dust cycle: 2. Simulation of Saharan dust sources, *J. Geophys. Res.*, *102*, 4387–4404.

Marticorena, B., P. Chazette, G. Bergametti, F. Dulac, and M. Legrand (2004), Mapping the aerodynamic roughness length of desert surfaces from the POLDER/ADEOS bi-reflectance product, *Int. J. Remote Sens.*, *25*, 603–626.

Messeh, M. A., and S. Quegan (2000), Variability in ERS scatterometer measurements over land, *IEEE Trans. Geosci. Remote Sens.*, *38*, 1767–1776.

Middleton, N. J. (1989), Climatic controls on the frequency, magnitude and distribution of dust storms: Examples from India/Pakistan, Mauritania, and Mongolia, in *Paleoclimatology and Paleometeorology: Modern and Past Patterns of Global Atmospheric Transport*, edited by M. Leinen and M. Sarnthein, pp. 97–132, Springer, New York.

Prospero, J. M., P. Ginoux, O. Torres, and S. E. Nicholson (2002), Environmental characteristics of global sources of atmospheric soil dust derived from the NIMBUS-7 TOMS absorbing aerosol product, *Rev. Geophys.*, *40*(1), 1002, doi:10.1029/2000RG000095.

Sellers, P. J., et al. (1997), Modeling the exchanges of energy, water, and carbon between the continents and the atmosphere, *Science*, *275*, 502–509.

Shao, Y. P. (2001), A model for mineral dust emission, *J. Geophys. Res.*, *106*, 20,239–20,254.

Shao, Y., M. R. Raupach, and J. F. Leys (1996), A model for predicting aeolian sand drift and dust entrainment on scales from paddock to region, *Aust. J. Soil Res.*, *34*, 309–342.

Tegen, I., and I. Y. Fung (1994), Modeling of mineral dust in the atmosphere: Sources, transport, and optical thickness, *J. Geophys. Res.*, *99*, 22,897–22,914.

Tegen, I., D. Koch, A. Lacis, and M. Sato (2000), Trends in tropospheric aerosol loads and corresponding impact on direct radiative forcing between 1950 and 1990: A model study, *J. Geophys. Res.*, *105*, 26,971–26,990.

Tegen, I., S. P. Harrison, K. E. Kohfeld, I. C. Prentice, M. C. Coe, and M. Heimann (2002), The impact of vegetation and preferential source areas on global dust aerosol: Results from a model study, *J. Geophys. Res.*, *107*(D21), 4576, doi:10.1029/2001JD000963.

Tegen, I., M. Werner, S. P. Harrison, and K. E. Kohfeld (2004), Relative importance of climate and land use in determining present and future global soil dust emission, *Geophys. Res. Lett.*, *31*, L05105, doi:10.1029/2003GL019216.

Wagner, W., K. Scipal, C. Pathe, D. Gerten, W. Lucht, and B. Rudolf (2003), Evaluation of the agreement between the first global remotely sensed soil moisture data with model and precipitation data, *J. Geophys. Res.*, *108*(D19), 4611, doi:10.1029/2003JD003663.

Wismann, V., K. Boehnke, and C. Schmullius (1993), Radar signatures of land surfaces measured by the ERS-1 scatterometer, paper presented at the 2nd ERS-1 Symposium, Eur. Space Agency, Hamburg, Germany.

Zender, C. S., D. Newman, and O. Torres (2003), Spatial heterogeneity in aeolian erodibility: Uniform, topographic, geomorphic, and hydrologic hypotheses, *J. Geophys. Res.*, *108*(D17), 4543, doi:10.1029/2002JD003039.

Zribi, M., O. Taconet, S. Le Hegarat-Mascle, D. Vidal-Madjar, C. Emblanch, and M. Normand (1997), Backscattering behavior and simulation: Comparison over bare soil using SIR-C/X-SA and ERASME 1994 data over Orgeval, *Remote Sens. Environ.*, *59*, 256–266.

Zribi, M., E. Adar, V. Ciarletti, J. C. Garcia, and O. Taconet (2003), Modelling of ERS 2 radar backscattering over rocky arid regions, *Int. J. Remote Sens.*, *24*, 5229–5242.

F. Aires, Laboratoire de Météorologie Dynamique, Ecole Polytechnique, CNRS/IPSL, F-91128 Palaiseau, France. (filipe.aires@lmd.polytechnique.fr)

B. Marticorena, Laboratoire Interuniversitaire de Systèmes Atmosphériques, UMR CNRS 7583, Universités Paris 7 et 12, 61, Avenue du Général de Gaulle, F-94010 Créteil, France.

C. Prigent, Centre National de la Recherche Scientifique, Laboratoire d'Etudes du Rayonnement et de la Matière en Astrophysique, Observatoire de Paris, 61, Avenue de l'Observatoire, F-75014 Paris, France. (catherine.prigent@obspm.fr)

I. Tegen, Max Planck Institute for Biogeochemistry, P.O. Box 100164, D-07701 Jena, Germany. (itegen@bgc-jena.mpg.de)

M. Zribi, Centre d'étude des Environnements Terrestre et Planétaires (CETP), 10-12 Avenue de l'Europe, F-78140 Vélizy, France. (zribi@cetp.ipsl.fr)